https://doi.org/10.5194/egusphere-2026-433
Preprint. Discussion started: 13 February 2026
© Author(s) 2026. CC BY 4.0 License.

Modeling and Experimental Validation of Rock Resistivity Evolution During Deformation up to Failure

Jianwei Ren[1,2,3], Lei Song[3,4], Haipeng Li[3], Xiangyang Jian[2], Pengfei Liang[2]

[1]Key Laboratory of Xinjiang Coal Resources Green Mining,Ministry of Education, Xinjiang Institute of Engineering, Urumqi, 830023, China
[2]School of Civil Engineering, Xinjiang Institute of Engineering, Urumqi, 830023, China
[3]State Key Laboratory of Intelligent Construction and Healthy Operation & Maintenance of Deep Underground Engineering, China University of Mining and Technology, Xuzhou, 221116, China
[4]YunLong Lake Laboratory of Deep Underground Science and Engineering, Xuzhou, 221116, China

Correspondence to: Lei Song (leisong@cumt.edu.cn)

Abstract. Modeling the evolution of rock resistivity during deformation up to failure is important for using resistivity to evaluate rock engineering properties related to rupture. In this paper, pores are classified into three types—elastic, perpendicular plastic, and parallel plastic pores—based on the evolution of pore geometry characteristics during rock fracture and the differing contributions of pore morphology to rock conductivity. In addition, a three-porosity rock resistivity model was established by incorporating Archie's formula. Based on the changing characteristics of the three types of rock pores under loading conditions, a pore volume evolution model under triaxial loading was derived using statistical damage theory. By combining the pore volume evolution model with the three-porosity rock resistivity model, a model for the evolution of rock resistivity during the triaxial loading rupture process was developed. Finally, the validity of the model was verified through experimental tests, and the influence of confining pressure on the model parameters was analyzed according to the test results.

1 Introduction

Fracture propagation is an important factor causing changes to the physical and mechanical properties of rocks, and identifying the development of fractures is crucial for engineering and geological disaster prevention. Rock resistivity is closely related to fracture development and has been widely used in earthquake and engineering disaster warning systems (Zhang et al. 2017; Nie et al. 2023). Modeling the evolution of resistivity during rock rupture under stress provides a more explicit correlation between stress and resistivity, significantly improving the accuracy of resistivity-based fracture identification.

As early as the 1960s, researchers studied changes in resistivity occurring in stress-damaged rocks under uniaxial and triaxial loading conditions (Parkhomenko and Bondarenko 1960; Brace et al. 1965), identifying for the first time the evolutionary characteristics of resistivity during fracture propagation. With advancements in testing methods, researchers began using high-density electrical methods to experimentally investigate the anisotropic characteristics of rock resistivity during loading

https://doi.org/10.5194/egusphere-2026-433
Preprint. Discussion started: 13 February 2026
© Author(s) 2026. CC BY 4.0 License.

(Chen et al. 2003). Subsequently, richer resistivity evolution data were obtained through resistivity tomography observations, enabling the analysis of differences in resistivity changes at different locations in rocks under stress (Falcon-Suarez et al. 2019). To complement micromechanism analyses, multiple testing methods combined with electrical resistivity—such as acoustic emission, ultrasound, and seismic signals—were employed to observe fracture development during rock damage (Katayama et al. 2023; Song et al. 2023;Oh 2013). These studies continue to deepen our understanding of the correlation between resistivity evolution and fracture extension. According to the observed trends in resistivity evolution under uniaxial loading conditions, Jia et al. (2020) proposed a resistivity-based characterization of rock fracture precursors.

Rocks are porous media, and predicting rock resistivity is a complex problem because of the intricate distribution of the solid and liquid phases. Archie first established a formula relating the overall resistivity of rocks to porosity and pore water resistivity (Archie 1942), which has few parameters and good applicability. Later, scholars broadened the applicability of Archie's formula to multiphase rocks through various modifications (Glover et al. 2000; Liu et al. 2022). With in-depth research into the micromechanisms of rock conductivity, the influence of pore structure on resistivity has garnered increasing attention. Through certain simplifications, researchers have developed curvature models (Attia 2005), double-porosity models (Clavier et al. 1984), pore throat models (Li et al. 2017), and fractal models (Rembert et al. 2020) that incorporate pore-conducting structures. To reflect the effect of pressure on rock resistivity, Qu et al. (2024) constructed an empirical equation relating uniaxial pressure and resistivity by fitting experimental data. Han (2018) derived a model for rock resistivity evolution under hydrostatic pressure based on the effective medium model.

Above literature reviews demonstrate that the evolution of resistivity during rock fracture has been extensively investigated both experimentally and theoretically, and several models describing the relationship between stress and resistivity have been developed. However, because existing models apply to stress conditions different from triaxial loading, they cannot accurately predict the evolution of rock resistivity during triaxial loading rupture.In this paper, we first analyzed the influence of different rock pore types on conductivity by considering the structural evolution of pores and fractures during triaxial rupture. Based on this analysis, we developed a three-porosity rock resistivity model. Considering the nonlinearity of rock pore deformation and the effect of effective stress, we subsequently formulated a rock pore volume evolution model under triaxial loading conditions using statistical damage theory. By combining the pore volume evolution model with the three-porosity rock resistivity model, we established an evolution model for rock resistivity during triaxial loading rupture. This theoretical framework was validated by comparing the experimental results of resistivity under different confining pressures.

2 Modeling basics

2.1 Archie's formula

By summarizing a large body of experimental data, Archie proposed an empirical formula for rock resistivity (Archie 1942). The fundamental principle can be expressed as follows: For pure, mud-free, and fully saturated rocks, the overall resistivity

https://doi.org/10.5194/egusphere-2026-433
Preprint. Discussion started: 13 February 2026
© Author(s) 2026. CC BY 4.0 License.

is proportional to the resistivity of the conductive fluid in the pores. This proportional coefficient is known as the formation factor (represented by F), which is a function of porosity (φ):

$$\rho_0/\rho_w = 1/\varphi^m = F \tag{1}$$

where ρ_0 is the resistivity of saturated rock, φ is the rock porosity, and ρ_w is the pore water resistivity. The parameter m is the cementation index and is typically obtained by fitting the F and φ values from experimental measurements. For the same rock, the cementation index m should remain constant, allowing changes in porosity to be inferred from changes in resistivity.

2.2 Pore evolution characteristics of rocks under triaxial loading

Changes in pore volume during triaxial loading result from a combination of microscopic processes, including fracture closure, pore elastic compression, fracture expansion, and fracture sliding (Li et al. 2017; Reches and Lockner 1994). A schematic diagram of each microprocess is shown in Fig. 1(a). Based on the characteristics of pore volume change during triaxial compression, the prepeak pore volume change curve can be divided into four stages: Stage I—initial compression; Stage II—linear compression; Stage III—fracture initiation and development; and Stage IV—rapid fracture expansion (Wang et al. 2016).

It is important to note that the proportion of each microprocess varies at different stages of loading. Germanovich and Dyskin (2000) experimentally found that crack initiation in triaxial loading is caused by tension rather than shear slip. Lockner et al. (1992) demonstrated this phenomenon through acoustic emission analysis, showing that specimens do not begin to shear until the stress level reaches approximately 70 percent of the peak strength. Therefore, fracture closure and pore elastic compression dominate the initial compression stage. The linear compression stage is primarily governed by pore elastic compression, while both pore elastic compression and fracture expansion contribute to the fracture initiation and development stage. During the rapid fracture expansion stage, fracture expansion and fracture sliding play dominant roles, although pore elastic compression remains present (Fig. 1[b]).

Both elastic and plastic deformation contribute to the total pore volume change. Elastic deformation is mainly caused by pore elastic compression, while fracture closure, expansion, and sliding result in plastic deformation. Furthermore, based on the stress conditions of the triaxial test, the closure and expansion of fractures during loading are known to be directional. In the initial phase of loading, primary fractures perpendicular or nearly perpendicular to the specimen's axial direction are compressed. Once stress exceeds a certain threshold, fractures parallel to the specimen's axial direction begin to crack and expand, continuing until specimen failure. Shear sliding occurs mostly parallel to the fracture surface and is primarily concentrated in the phase just before specimen failure (Healy et al 2006).

https://doi.org/10.5194/egusphere-2026-433
Preprint. Discussion started: 13 February 2026
© Author(s) 2026. CC BY 4.0 License.

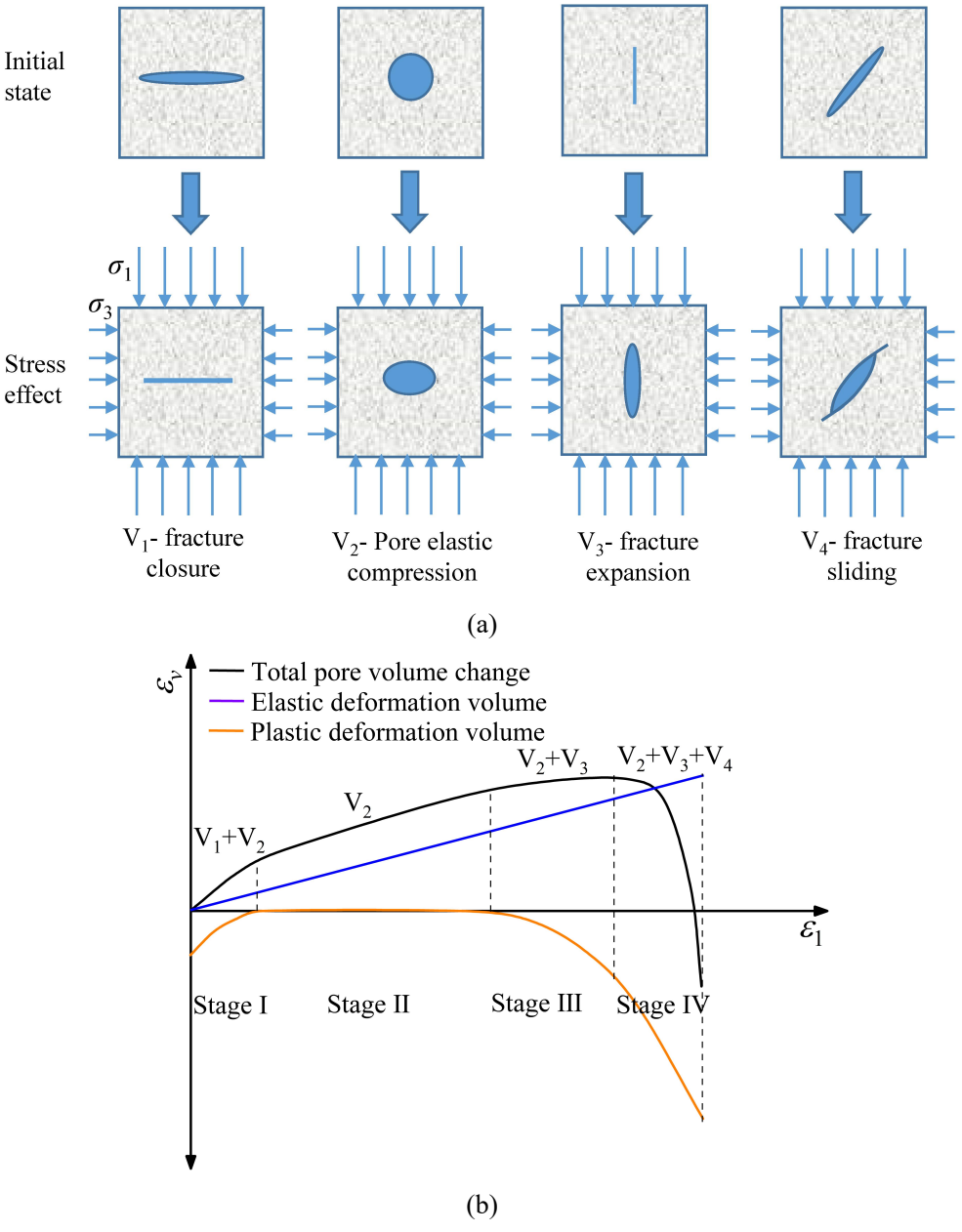

Figure 1. Schematic diagram of the evolution of rock pore volume under triaxial loading: (a) microprocess of pore volume change; (b) segmented characteristics of pore volume changes.

2.3 Dual porosity model

In the initial compression stage, changes in pore volume result from pore elastic compression and fracture closure. Since fractures are more easily compressed than pores, fractures and pores exhibit different patterns of change under stress.

https://doi.org/10.5194/egusphere-2026-433
Preprint. Discussion started: 13 February 2026
© Author(s) 2026. CC BY 4.0 License.

Shapiro (2005) suggested that pore volume decreases linearly with increasing stress, whereas fracture volume decreases exponentially with increasing stress:

$$\varphi_h(\sigma_e)=(1-\gamma)\varphi_0-\sigma_e(C_{ds}-C_g) \tag{2}$$

$$\varphi_s(\sigma_e)=\gamma\varphi_0\exp(-\lambda C_{ds}\sigma_e) \tag{3}$$

where φ_h and φ_s are the porosity of rock pores and primary fractures, respectively; σ_e is the effective stress, defined as the difference between the total stress and pore pressure; φ_0 is the initial porosity when the rock is not under stress; γ is the proportion of primary fractures in the initial porosity; C_{ds} is the compression coefficient of rock; C_g is the compression coefficient of rock minerals; and λ is the pressure sensitivity coefficient of the primary fractures. For rock, given that C_g is much smaller than C_{ds}, it can be ignored. At this point, the change in pore volume is equal to the elastic deformation of the rock. According to generalized Hooke's law, C_{ds} can be expressed as

$$C_{ds}=\frac{3(1-2\mu)}{E} \tag{4}$$

where E is the elastic modulus of the rock (GPa) and μ is Poisson's ratio. The pore deformation can be expressed as follows:

$$\varphi_h(\sigma_e)=\varphi_{h0}-\sigma_e C_{ds}=(1-\gamma)\varphi_0-\frac{3\sigma_e(1-2\mu)}{E} \tag{5}$$

As the deformation of primary fractures occurs mainly along the direction of force, the influence of Poisson's ratio can be neglected. The deformation of primary fractures can thus be simplified as follows:

$$\varphi_s(\sigma_e)=\gamma\varphi_0\exp\left(-\frac{3\lambda\sigma_e}{E}\right) \tag{6}$$

3 Model building

3.1 Three-porosity rock resistivity model

In Archie's formula, m is an important parameter representing the pore conductive connectivity. However, triaxial rock resistivity tests indicate that m varies with changes in effective stress (Brace and Orange 1968). This suggests that the relationship between the formation factor and total porosity no longer satisfies the application conditions of Archie's formula. Since pore plastic deformation is the main factor causing changes in pore conductive connectivity (Jia et al. 2020), it is necessary to distinguish between the effects of elastic and plastic pore deformation in resistivity modeling. Moreover, differences exist in the directional arrangement of plastic pores between triaxial loading Stage I and Stages III and IV. To account for this effect, plastic pores are divided into parallel and perpendicular directions for simplicity. The final rock conductivity model consists of three components: elastic pores, parallel plastic pores, and perpendicular plastic pores. A schematic diagram of the model is shown in Fig. 2.

https://doi.org/10.5194/egusphere-2026-433
Preprint. Discussion started: 13 February 2026
© Author(s) 2026. CC BY 4.0 License.

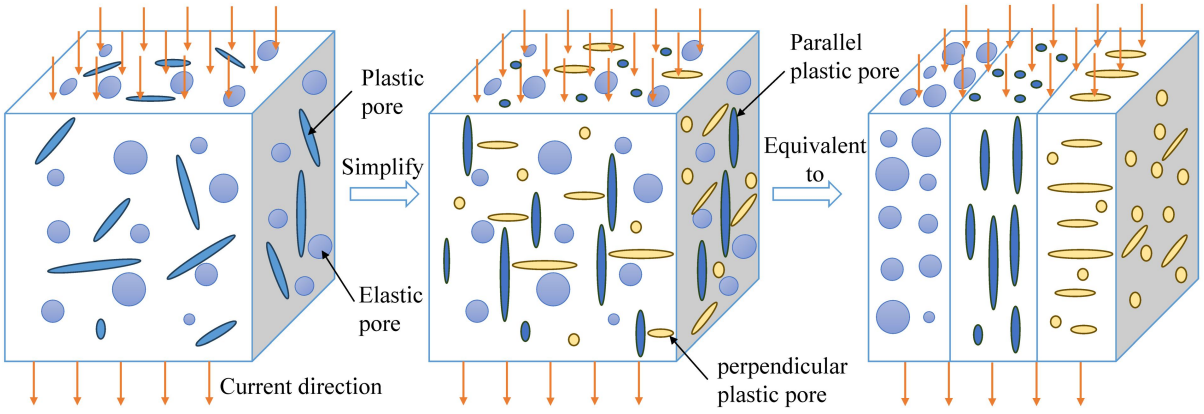

Figure 2. Schematic diagram of a three-pore rock conductivity model considering directionality.

The three types of pores are considered to be in parallel in terms of conductivity:

$$\frac{1}{R_0}=\frac{1}{R_e}+\frac{1}{R_h}+\frac{1}{R_v} \tag{7}$$

where R_0 is the total resistance of the rock (Ω), R_e is the resistance of the elastic pores (Ω), R_h is the resistance of the parallel plastic pores (Ω), and R_v is the resistance of the perpendicular plastic pores (Ω). According to the law of resistance, Eq. (7) can be rewritten to relate the total rock resistivity to the resistivity of each part:

$$\frac{1}{\rho_0}=\frac{1}{\rho_e}+\frac{1}{\rho_h}+\frac{1}{\rho_v} \tag{8}$$

where ρ_e is the resistivity of elastic pores (Ω·m), ρ_h is the resistivity of parallel plastic pores (Ω·m), and ρ_v is the resistivity of perpendicular plastic pores (Ω·m).

Substituting Eq. (6) into Eq. (8) yields the expression for rock resistivity in relation to each porosity:

$$\frac{\rho_w}{\rho_0}=\varphi_e^{m_e}+\varphi_h^{m_h}+\varphi_v^{m_v} \tag{9}$$

where φ_e, φ_h, and φ_v represent the porosity of elastic pores, parallel plastic pores, and perpendicular plastic pores, respectively, and m_e, m_h, and m_v are the cementation indices of the three types of pores, respectively. For rocks under triaxial loading, φ_e, φ_h, and φ_v correspond to the pore volume, primary fracture volume, and cracked fracture volume, respectively.

3.2 Pore volume evolution model

Obtaining the porosity of the three types of pores during triaxial loading is key to calculating resistivity. The dual porosity model can only account for changes in pore volume during Stages I and II and does not reflect changes in plastic pore volume during Stages III and IV. In reality, an increase in plastic pore volume because of loading is a process of continuous rock damage and destruction. Therefore, we used statistical damage models to calculate the extent of rock damage under

https://doi.org/10.5194/egusphere-2026-433
Preprint. Discussion started: 13 February 2026
© Author(s) 2026. CC BY 4.0 License.

different stresses and establish the relationship between pore volume and stress during triaxial loading by introducing Rowe's shear expansion equation.

3.2.1 Statistical damage constitutive model

Current damage models for rocks are primarily based on the Lemaitre strain equivalence hypothesis (Lemaitre 1984):

$$\bar{\sigma}_{ij}=\sigma'_{ij}(1-D) \tag{10}$$

where σ'_{ij} is the effective stress tensor, $\bar{\sigma}_{ij}$ is the nominal effective stress tensor, and D is the damage variable. The damage variable is defined here as the ratio of the number of microelements N_t that have been destroyed in the rock to the total number of microelements N:

$$D=\frac{N_t}{N} \tag{11}$$

For porous materials such as rocks, the hydraulic coupling effect is usually described by the effective stress equation (Terzaghi 1936). Its expression is as follows:

$$\bar{\sigma}_{ij}=\sigma_{ij}-P_w\delta_{ij} \tag{12}$$

where σ_{ij} is the stress tensor, P_w is the pore water pressure, and δ_{ij} is the unit second-order tensor, with δ_{ij}=1 when i=j and δ_{ij}=0 when i≠j. By combining Eq.s (12) and (10), the effective stress tensor under hydraulic coupling can be expressed as follows:

$$\sigma'_{ij}=\frac{\sigma_{ij}-P_w\delta_{ij}}{1-D} \tag{13}$$

The physical meaning of Eq. (10) is that the total stress in the rock is borne by the undamaged part. For undamaged rock microelements, their deformation follows the generalized Hooke's law, which under triaxial loading conditions is given by

$$\sigma'_1=E\varepsilon'_1+\sigma'_3 \tag{14}$$

where E and μ are the modulus of elasticity and Poisson's ratio of undamaged rock, respectively, and ε_1' is the microscopic strain in the undamaged part of the rock caused by deviatoric stress.

Under conventional triaxial loading conditions, it is assumed that rock damage occurs only in the axial direction and that no damage occurs in the horizontal direction. In other words, the nominal stress is equal to the effective stress in the horizontal direction. From the deformation coordination relation, it follows that the macroscopic strain ε_1 of the rock material is equal to the microscopic strain ε'_1 of the undamaged part:

https://doi.org/10.5194/egusphere-2026-433
Preprint. Discussion started: 13 February 2026
© Author(s) 2026. CC BY 4.0 License.

$$\begin{cases} \sigma_2'=\sigma_2-p_w \\ \sigma_3'=\sigma_3-p_w \\ \varepsilon_1'=\varepsilon_1 \end{cases} \tag{15}$$

Therefore, the damage model for rock under triaxial conditions can be expressed as follows:

$$\sigma=(E\varepsilon_1+\sigma_3-P_w)(1-D)+P_w \tag{16}$$

Rock damage is a continuous process in which the degree of damage to the rock gradually increases as loading increases. The strength distribution of rock microelements determines how the damage variables vary with stress. Here, it is assumed that the rock microelement strength follows a Weibull distribution, with its probability density function $P(F)$ given as

$$P(F)=\frac{n}{F_0}\left(\frac{F}{F_0}\right)^{n-1}\exp\left[-\left(\frac{F}{F_0}\right)^n\right] \tag{17}$$

where F_0 and n are the Weibull distribution parameters, which reflect the mechanical properties of the rock, and F is the random distribution variable of the rock microelement strength. The strength of rock is related to the stress to which it is subjected. The equation that describes the relationship between rock strength and stress is called the strength criterion. In this paper, the Mohr–Coulomb criterion is used to determine the rock strength:

$$F=\sigma_1'-\sigma_3'-\left(\sigma_1'+\sigma_3'\right)\sin\theta=2C\cos\theta \tag{18}$$

where θ and C are the internal friction angle and cohesive force of the rock, respectively. If F is expressed in nominal stress, it becomes

$$F=\frac{\sigma_1-p_w}{1\text{-}D}-(\sigma_3-p_w)-\left(\frac{\sigma_1-p_w}{1\text{-}D}+(\sigma_3-p_w)\right)\sin\theta \tag{19}$$

According to Eq. (16), it follows that $1\text{-}D=(\sigma_1\text{-}p_w)/(E\varepsilon_1+\sigma_3-p_w)$. Substituting this into equation (19) yields

$$F=E\varepsilon_1-\left(E\varepsilon_1+2(\sigma_3-P_w)\right)\sin\theta \tag{20}$$

From its definition, the damage variable for rock at a given stress level can be expressed as follows:

$$D=\int_0^F P(F)dx=1-\exp[-(\frac{F}{F_0})^n] \tag{21}$$

By substituting Eq. (21) into Eq. (16), the statistical damage constitutive equation for rock can be obtained as follows:

$$\sigma=\begin{cases}(E\varepsilon_1+\sigma_3-P_w)\exp\left[-(\frac{F}{F_0})^n\right]+P_w & F\geq 0 \\ E\varepsilon_1+\sigma_3 & F<0\end{cases} \tag{22}$$

https://doi.org/10.5194/egusphere-2026-433
Preprint. Discussion started: 13 February 2026
© Author(s) 2026. CC BY 4.0 License.

Because of the presence of primary fractures, the triaxial compression curve in the initial compression stage is nonlinear, and the stress-strain relationship at this stage cannot be described by Hooke's law. If the nonlinear deformation in the initial stage is not considered in the stress-strain relationship described in Eq. (22), the calculated stress will be overestimated. Therefore, it is necessary to account for the influence of primary fracture compression deformation. The primary fracture deformation of rocks in the initial stage of triaxial compression can be calculated using Eq. (6). Assuming that the rock is isotropic, the compressive deformation of primary fractures caused by deviatoric stress under triaxial loading is one-third of the compressive deformation of primary fractures caused by hydrostatic pressure of the same magnitude:

$$\varepsilon_s = \frac{1}{3}\varphi_s(\sigma_e) = \frac{1}{3}\gamma\varphi_0 \exp\left(-\frac{3\lambda\sigma_e}{E}\right) = \frac{1}{3}\gamma\varphi_0 \exp\left(-\frac{3\lambda(\sigma_1-\sigma_3)}{E}\right) \tag{23}$$

Substituting Eq. (23) into Eq. (22) yields the statistical damage constitutive equation for rock considering the initial compression stage:

$$\sigma = \begin{cases} \left[E(\varepsilon_1 - \frac{\gamma\varphi_0}{3}) + \sigma_3 - P_w\right]\exp\left[-(\frac{F}{F_0})^n\right] + P_w & F \geq 0 \\ E(\varepsilon_1 - \varepsilon_s) + \sigma_3 & F < 0 \end{cases} \tag{24}$$

3.2.2 Calculation of rock porosity

Since the stiffness of the rock is much smaller than the stiffness of the rock minerals, rock deformation is considered here to be equal to the change in pore volume. This change can be obtained by calculating the bulk strain of the rock. As described in Section 2.2, the prepeak pore volume change is divided into four stages according to the characteristics of the change in pore volume. For the undamaged portion of the rock across all stages, the bulk strain can be calculated using Eq. (5). In Stage I, the plastic volume compression of the rock can be calculated using Eq. (6). In Stages II and III, the volume change of the damaged portion of the rock is obtained by introducing Rowe's shear expansion equation.

Once the rock reaches the damage stage, the bulk strain begins to change nonlinearly because of the expansion of the damaged rock units under stress. Deformation in the damage stage consists of two components: elastic compression of the undamaged rock unit and shear expansion of the damaged unit. The overall deformation of the rock is the superposition of these two components:

$$d\varepsilon_v = \frac{V^e}{V}d\varepsilon_v^e + \frac{V^p}{V}d\varepsilon_v^p = (1-D)d\varepsilon_v^e + Dd\varepsilon_v^p \tag{25}$$

where V is the total volume of the rock, V^e is the volume of the undamaged part, and V^p is the volume of the damaged part, such that $V=V^e+V^p$. According to the definition of damage variables, it follows that $V^p/V=D$; ε_v^e is the bulk strain of the undamaged component and can be calculated using Eq. (5), while ε_v^p is the bulk strain of the damaged part. In this paper,

https://doi.org/10.5194/egusphere-2026-433
Preprint. Discussion started: 13 February 2026
© Author(s) 2026. CC BY 4.0 License.

Rowe's shear expansion equation is used to describe the relationship between plastic bulk strain and axial strain (Rowe 1962):

$$\frac{d\varepsilon_v^p}{d\varepsilon_1^p}=1-\frac{\sigma_1}{\sigma_3}\cdot\frac{1}{\tan^2(\frac{\pi}{4}+\frac{\theta_u}{2})} \tag{26}$$

where θ_u is the sliding friction angle of the rock and ε_1^p is the strain in the direction of the major principal stress. From deformation coordination, it follows that $\varepsilon_1^p=\varepsilon_1$. The increment of plastic bulk strain is obtained by transforming the above equation:

$$d\varepsilon_v^p=\left[1-\frac{\sigma_1}{\sigma_3}\cdot\frac{1}{\tan^2(\frac{\pi}{4}+\frac{\varphi_u}{2})}\right]d\varepsilon_1 \tag{27}$$

To simplify the derivation of the constitutive equations, it is assumed that the damaged component does not bear stress, meaning $\sigma_1=\sigma_3$. If this assumption is applied to calculating the plastic deformation, then ε_v^p will have a constant positive value, which is not consistent with reality. In fact, the damaged rock unit retains some residual strength, which can be used to represent the magnitude of the principal stress in the damaged rock. We denote $1\text{-}\sigma_1/\sigma_3\tan^2(\frac{\pi}{4}+\frac{\theta_u}{2})=u$ as the coefficient of expansion. Typically, the residual strength can be considered constant (Li et al. 2018), making the expansion coefficient u constant for the damaged unit. By integrating Eq. (27), the plastic strain of the damaged rock unit can be obtained:

$$\varepsilon_v^p=\int\left[1-\frac{\sigma_1}{\sigma_3}\cdot\frac{1}{\tan^2(\frac{\pi}{4}+\frac{\theta_u}{2})}\right]d\varepsilon_1=\int u\frac{d\sigma_1'}{E}=\frac{u}{E}\Big|_{\sigma_1'^s}^{\sigma_1'} \tag{28}$$

where $\sigma_1'^s$ is the effective stress corresponding to the initial failure of the rock unit. Assuming that the residual strength of the damaged unit is proportional to its strength (i.e., $\sigma_1'^s/u$ is a constant), then the value of u is different for rock units of different strengths. The coefficient of expansion at peak stress is noted as $u=u_m$. For units with a strength of $\sigma_1'^s$, their expansion coefficient is $u=u_s=\frac{\sigma_1'^s u_m}{\sigma_1'^p}$. We substitute u_s into Eq. (28) to obtain the plastic strain of the rock element from the onset of damage to an effective stress σ_1':

https://doi.org/10.5194/egusphere-2026-433
Preprint. Discussion started: 13 February 2026
© Author(s) 2026. CC BY 4.0 License.

$$\varepsilon_v^{ps} = \frac{(\sigma_1' - \sigma_1'^s)\sigma_1'^s u_m}{E\sigma_1'^p} \tag{29}$$

Since the strength of each unit varies, the plastic strain of each failed rock unit differs when the effective stress is σ_1'. The total plastic strain of the rock is the superposition of the product of the volume fraction of each unit and its plastic strain:

$$\varepsilon_v^p = \int_0^{D'} \varepsilon_v^{ps} dD = \int_0^{D'} \frac{(\sigma_1' - \sigma_1'^s)\sigma_1'^s u_m}{E\sigma_1'^p} dD \tag{30}$$

where D' is the damage value of the rock corresponding to the effective stress σ_1'. According to Eq. (18) and (21), σ_1' and D can be expressed in terms of F. Therefore, the plastic strain of the rock can be written as

$$\begin{aligned}\varepsilon_v^p &= \int_0^{F'} \frac{u_m(F'-F)\left[F+\sigma_3'(1+\sin\theta)\right]}{E\sigma_1'^p(1-\sin\theta)^2}\exp\left[-(\frac{F}{F_0})^n\right]\cdot\frac{nF^{n-1}}{F_0^n}dF \\ &= \frac{-u_m F'\sigma_3'(1+\sin\theta)\exp\left[-(\frac{F}{F_0})^n\right] + u_m F_0^2 A + u_m\left[\sigma_3'(1+\sin\theta)-F'\right]F_0 B}{E\sigma_1'^p(1-\sin\theta)^2}\end{aligned} \tag{31}$$

where A and B are gamma functions with the following expressions:

$$A = \Gamma(\frac{n+2}{n}, \frac{F^n}{F_0^n}) \tag{32}$$

$$B = \Gamma(\frac{n+1}{n}, \frac{F^n}{F_0^n}) \tag{33}$$

3.2.3 Values of model parameters

The unknown parameters in the model are F_0, n, and u_m. The extreme value characteristics of the peak points are used to determine these parameters. The corresponding principal stress, principal strain, and bulk strain at the peak point of the rock's stress-strain curve are denoted as σ_{1p}, ε_{1p}, and ε_{vp}, respectively, with the microelement strength represented as F_p. When $\varepsilon_1=\varepsilon_{1p}$, then $\sigma_1=\sigma_{1p}$:

$$\sigma_{1p} = (E\varepsilon_{1p} + \sigma_3 - P_w)\exp\left[-(\frac{F_p}{F_0})^n\right] + P_w \tag{34}$$

At the peak point, the partial derivative of σ_1 with respect to ε_1 in Eq. (24) is zero, yielding

https://doi.org/10.5194/egusphere-2026-433
Preprint. Discussion started: 13 February 2026
© Author(s) 2026. CC BY 4.0 License.

$$\frac{\partial\sigma_1}{\partial\varepsilon_1}=E\exp\left[-\left(\frac{F_p}{F_0}\right)^n\right]+(E\varepsilon_1+\sigma_3-P_w)\exp\left[-\left(\frac{F_p}{F_0}\right)^n\right]\cdot\left(-n\frac{F_p^{\,n-1}}{F_0^{\,n}}\right)\cdot\left[(1-\sin\varphi)E\right]=0 \tag{35}$$

Combining Eq. (34) and (35) gives the expressions for F_0 and n:

$$n=\frac{-F_P}{\left[E(\varepsilon_{1p}-\frac{\gamma\varphi_0}{3})+\sigma_3-P_w\right](1-\sin\varphi)\ln\frac{\sigma_{1p}-P_w}{\left[E(\varepsilon_{1p}-\frac{\gamma\varphi_0}{3})+\sigma_3-P_w\right]}} \tag{36}$$

$$F_0=\frac{F_p}{\left(-\ln\frac{\sigma_{1p}-P_w}{\left[E(\varepsilon_{1p}-\frac{\gamma\varphi_0}{3})+\sigma_3-P_w\right]}\right)^{\frac{1}{n}}} \tag{37}$$

The expression for u_m can be obtained by writing σ_1 in terms of F according to Eq. (18) and substituting it into Eq. (31):

$$u_m=\frac{\left[E\varepsilon_{vp}-(1-2\mu)(\sigma_1-\sigma_3)\right]\left[F_p+\sigma_3(1+\sin\theta)\right](1-\sin\theta)}{F_0^{\,2}A-F_p\sigma_3(1+\sin\theta)+B\left[\sigma_3(1+\sin\theta)-F_p\right]} \tag{38}$$

3.3 Evolution model of rock resistivity during triaxial loading rupture

A three-porosity resistivity model that takes into account the directionality of the rock pores and a pore volume evolution model were developed in Sections 3.1 and 3.2, respectively. According to the stress conditions of the rock, the elastic and plastic porosities in the perpendicular and parallel directions can be calculated from the pore volume evolution model. These values can then be incorporated into the three-porosity resistivity model to obtain the rock resistivity evolution model. Because of the involvement of multiple parameters, the model is represented by the following system of equations:

https://doi.org/10.5194/egusphere-2026-433
Preprint. Discussion started: 13 February 2026
© Author(s) 2026. CC BY 4.0 License.

$$\begin{cases} \rho = \dfrac{\rho_w}{\varphi_e^{m_e} + \varphi_h^{m_h} + \varphi_v^{m_v}} \\ \varphi_h = \dfrac{\gamma\varphi_0}{3}\exp\left(-\dfrac{3\lambda(\sigma_1-\sigma_3)}{E}\right) \\ \varphi_e = (1-\gamma)\varphi_0 - \dfrac{(1-2\mu)(\sigma_1-\sigma_3)}{E} \\ \varphi_v = \dfrac{2\gamma\varphi_0}{3} + \dfrac{-u_m F'\sigma_3'(1+\sin\theta)\exp\left[-(\dfrac{F}{F_0})^n\right] + u_m F_0^{\,2} A + u_m\left[\sigma_3'(1+\sin\theta) - F'\right]F_0 B}{E\sigma_1'^{\,p}(1-\sin\theta)^2} \end{cases} \tag{39}$$

4 Experimental validation of the model

The new model in this paper characterizes the dynamic evolution of resistivity in rocks during the process from deformation to failure, so the model contains some parameters of rock damage mechanics (e.g., E, F_0, n); it also embodies the difference between elastic and plastic pores in terms of electrical conductivity, so the model contains parameters related to pore volume (e.g., φ_0, γ, u_m). These parameters could not all be found in previous studies. Therefore, we did several sets of resistivity tests during triaxial loading to verify the accuracy of the model.

Test materials and methods

The specimens were made of limestone and cut into cylinders with a diameter of 50 mm and a height of 100 mm. The limestone had a density of 2.74 g/cm^3 and porosity of 0.75%. The composition of the rock was measured by XRD, showing that calcite accounted for 70.0%, dolomite for 8.4%, illite for 9.3%, and quartz for 12.3%.

The experiments were carried out using a multifield rock resistivity testing system developed by the China University of Mining and Technology (Ren et al. 2023). This system can apply a confining pressure of up to 30 MPa, a pore pressure of up to 20 MPa (achieved through salt solution injection via a piston container), and maintain a temperature range of 0–80°C. Resistivity measurements were conducted using the two-electrode method. The total resistance of the sample was measured with a digital bridge, and the average resistivity of the rock between the electrodes was determined using Ohm's law. To avoid electrode polarization, a test frequency of 100 Hz was employed. The schematic diagram of the resistivity test system is shown in Fig. 3.

https://doi.org/10.5194/egusphere-2026-433
Preprint. Discussion started: 13 February 2026
© Author(s) 2026. CC BY 4.0 License.

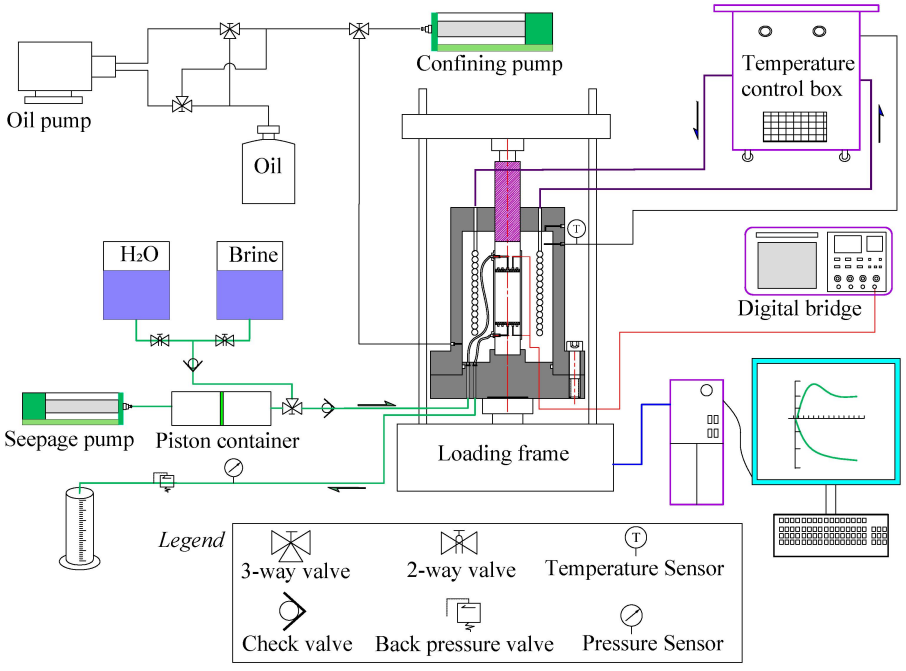

Figure 3. Schematic diagram of the resistivity testing system (Ren et al. 2023).

Triaxial consolidation drainage tests were carried out on limestone specimens under four different confining pressures (P_c=5 MPa, 10 MPa, 15 MPa, and 20 MPa) with a pore pressure of 3 MPa at a temperature of 20°C. During the experiment, the pore pressure was kept constant, and changes in the pore volume of the specimen were measured by recording the volume change in the pore pressure pump. The axial and radial deformations of the specimen were measured using strain gauges attached to the side of the specimen.

4.2 Test results

4.2.1 Pore volume change

The change in the volume of water in the pore pressure pump was recorded during the test. Since the sample was saturated, a change in seepage pump volume was used to represent the pore volume change. The variation in the pore volume of the specimens during loading is shown in Fig. 4(a), where pore compression is taken as positive.

It can be seen that the pore volume changes under different confining pressures exhibit similar patterns. Initially, the pore volume decreases rapidly, followed by a linear decrease. When the pressure reaches a certain threshold, the rate of decrease in pore volume gradually slows, and the curve takes on an upward convex shape. Finally, the pore volume reaches a minimum value before increasing rapidly. The characteristics of the measured pore volume changes in this study are consistent with previous research (Wang et al. 2016), allowing the pore volume-deviatoric stress curves to be divided into four stages, as illustrated in Fig. 4(b).

https://doi.org/10.5194/egusphere-2026-433
Preprint. Discussion started: 13 February 2026
© Author(s) 2026. CC BY 4.0 License.

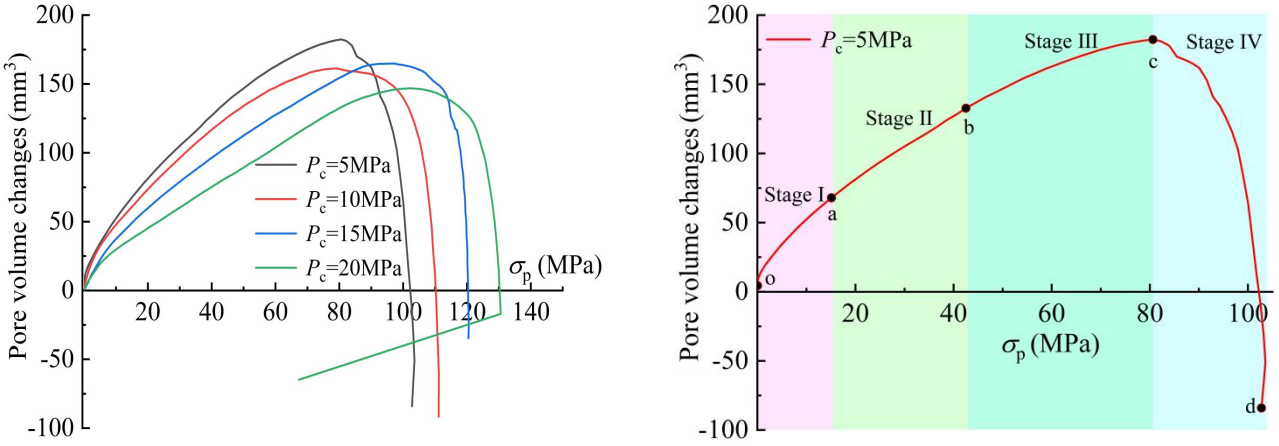

Figure 4. Pore volume-stress curves of limestone under triaxial loading conditions: (a) test results at different confining pressures; (b) schematic diagram of the stage division.

4.2.2 Resistivity change

Fig. 5(a) shows the relationship between resistivity and deviatoric stress in limestone under different confining pressures. The variation in resistivity with deviatoric stress follows trends similar to those found in previous studies (Brace and Orange 1968). Based on these characteristics, the resistivity curve during the triaxial process can also be divided into four stages, as illustrated in Fig. 5(b).

During Stage A, when the sample is subjected to axial deviatoric stress, the pores are compressed and the primary fractures close. This process squeezes the conductive channels of the specimen, leading to a slight nonlinear increase in resistivity. In Stage B, the primary fractures are almost completely closed, and the deformation of the specimen is primarily because of the elastic compression of the pores. At this point, the resistivity changes in direct relation to pore volume, exhibiting an approximately linear variation. In Stage C, when stress reaches the fracture initiation threshold, new fractures begin to develop within the rock. These newly formed cracks increase the connectivity of pore water, leading to a gradual decrease in the rate of resistivity increase. As the number of fractures continues to grow in Stage D, the resistivity reaches its maximum value. With further fracture expansion, the resistivity begins to decline. During the rapid fracture expansion stage, the resistivity decreases sharply, and at peak stress, the specimen resistivity is significantly lower than its initial value.

https://doi.org/10.5194/egusphere-2026-433
Preprint. Discussion started: 13 February 2026
© Author(s) 2026. CC BY 4.0 License.

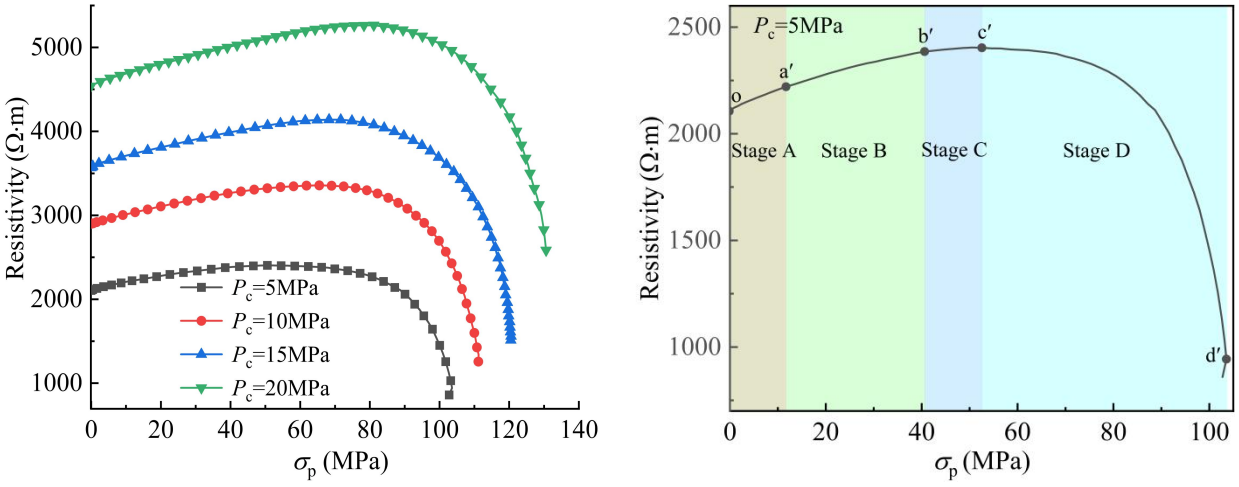

Figure 5. Resistivity-stress curve of limestone under triaxial loading conditions: (a) test results at different confining pressures; (b) schematic diagram of the stage division.

4.2.3 Resistivity change vs. porosity change

Figure 6 shows the variation curves of rock resistivity and pore volume during triaxial loading. A close correlation can be observed between the change of resistivity and the change of pore volume. The resistivity changes in Stages A and B correspond closely to Stages I and II of the pore volume change, respectively. The rate of resistivity increase begins to slow when plastic cracking occurs in the rock pores; however, the peak resistivity point, denoted as c', tends to occur before the pore volume minimum, denoted as c. This discrepancy arises because the resistivity of saturated rock is influenced not only by changes in pore volume but also by changes in pore connectivity.

In Stages III and IV, pore volume changes result from both pore compression, which decreases pore volume, and fracture expansion, which increases pore volume and enhances connectivity. The resistivity observed is a combined effect of these opposing processes. In the early phase of fracture development, the increase in fracture volume is relatively small compared to the pore volume compression. As a result, the decrease in resistivity caused by fracture formation is less significant than the increase in resistivity caused by pore compression. Overall, resistivity continues to increase, but the rate of increase gradually declines as deviatoric stress rises. When the fracture expansion reaches a critical level, the effect of increasing fractures on resistivity exceeds the effect of pore compression, leading to a gradual decline in resistivity.

https://doi.org/10.5194/egusphere-2026-433
Preprint. Discussion started: 13 February 2026
© Author(s) 2026. CC BY 4.0 License.

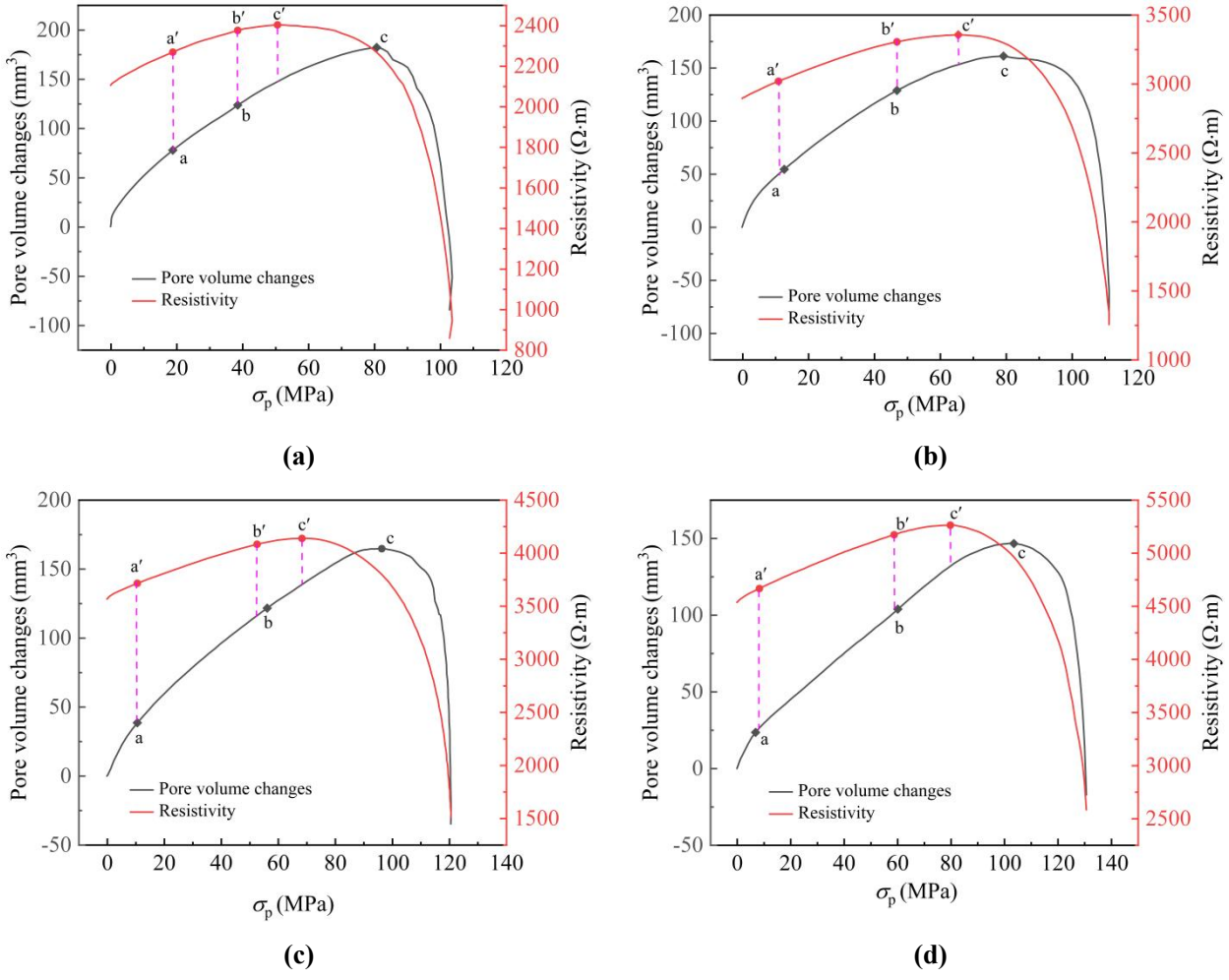

Figure 6. Curves of limestone resistivity and pore volume change during triaxial loading: (a) P_c=5 MPa; (b) P_c=10 MPa; (c) P_c=15 MPa; (d) P_c=20 MPa.

4.3 Model validation

Based on the stress and deformation data measured during the tests, the parameters of the resistivity evolution model were calculated for each test condition, as shown in Table 1. By substituting the experimentally obtained model parameters into Eq. (39), the variation in rock resistivity under different experimental conditions was determined. A comparison of the calculated results with the experimental data is shown in Fig. 7. The model curve exhibits strong concordance with the observed experimental trends, indicating that the rock resistivity model based on porosity evolution is effective and accurately reflects the evolution law of rock resistivity under stress.

Table 1 Parameters of the resistivity evolution model under triaxial loading

https://doi.org/10.5194/egusphere-2026-433
Preprint. Discussion started: 13 February 2026
© Author(s) 2026. CC BY 4.0 License.

Testing conditions	n	F_0 (MPa)	u_m	φ_0 (%)	γ	E (GPa)
P_c=5 MPa	1.92	126.95	-3.60	0.66	0.028	43.64
P_c=10 MPa	1.31	150.58	-1.72	0.60	0.033	49.63
P_c=15 MPa	1.20	164.95	-1.30	0.56	0.027	55.21
P_c=20 MPa	0.82	185.29	-0.45	0.52	0.019	59.41

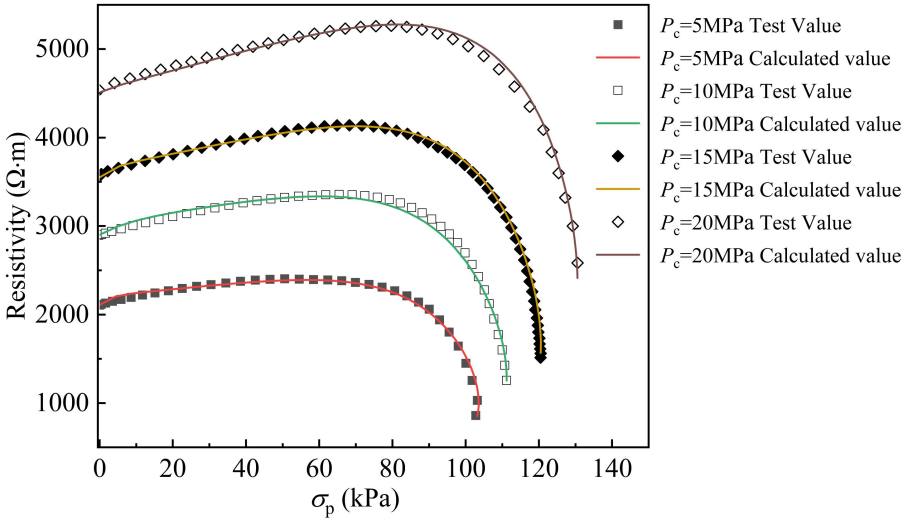

Figure 7. Observed and calculated resistivity curves for different confining pressures, illustrating model accuracy across stress conditions.

5 Parameter analysis

The rock resistivity evolution model derived in this paper is based on the three-porosity resistivity model, which accounts for the differing contributions of various pore types to the overall conductivity of rock. The cementation index m is an important parameter in the model, representing the strength of conductive connectivity among different pore types. The values of m_e, m_h, *and* m_v under different experimental conditions were obtained by fitting the experimental data, as shown in Table 2.

The parameter m_h increases gradually with confining pressure. This is because the primary fractures in the rock are compressed under higher confining pressure, reducing their connectivity and leading to an increase in the cementation index. Similarly, m_v also increases with increasing confining pressure, suggesting that the influence of fracture expansion on changes in rock conductivity connectivity is weaker at higher confining pressures. Although the fractures formed in triaxial loading are simplified as being parallel to the direction of the principal stress in the model, in reality, fracture extension exhibits a certain degree of inclination. Based on their study of acoustic emission moment tensors, Chang and Lee (2004) found strong agreement between the statistical average of fracture inclination and the inclination of the rupture surface of the

https://doi.org/10.5194/egusphere-2026-433
Preprint. Discussion started: 13 February 2026
© Author(s) 2026. CC BY 4.0 License.

specimen. As the latter increases with increasing confining pressure, the contribution of fractures to resistivity in the axial direction of the specimen weakens at higher confining pressures. The value of m_e remains constant at 1.73 across all test conditions, indicating that confining pressure has little effect on the conductive connectivity of the pores.

Table 2 Cementation index of the specimens under each test condition

Testing conditions	m_e	m_h	m_v
P_c=5 MPa	1.73	1.33	1.275
P_c=10 MPa	1.73	1.37	1.280
P_c=15 MPa	1.73	1.40	1.290
P_c=20 MPa	1.73	1.50	1.322

6 Conclusions

In this paper, a three-porosity resistivity model was proposed by considering changes in pore geometry characteristics during the rock rupture process. The volume changes of the three types of pores under triaxial loading were derived, leading to the development of a rock resistivity evolution model for triaxial rupture.

The main conclusions are as follows:

(1) The three-porosity resistivity model divides the rock pores into elastic pores, parallel plastic pores, and perpendicular plastic pores. The overall resistivity is treated as a parallel connection of the resistivities of these three pore types. This model effectively captures the morphological and volumetric changes in pores and fractures during the triaxial loading rupture process, as well as the conductive mechanisms of saturated rock.

(2) Based on the micromechanism of pore volume changes at different stages of the triaxial rupture process in rock and using statistical damage theory, the expressions for elastic pores, parallel plastic pores, and perpendicular plastic pores under triaxial loading were derived. By substituting these expressions into the three-porosity model, the evolution model of rock resistivity during triaxial rupture was obtained. The validation results demonstrate that the model effectively captures the resistivity evolution behavior of rock under triaxial rupture conditions.

This model was developed under the assumption of rock saturation. Therefore, its applicability to unsaturated rocks requires further verification.

Author contributions

Jianwei Ren: Methodology, Investigation, Writing- Original draft preparation. Lei Song: Conceptualization, Data curation, Funding acquisition. Haipeng Li: Writing-Reviewing and Editing, Visualization.

https://doi.org/10.5194/egusphere-2026-433
Preprint. Discussion started: 13 February 2026
© Author(s) 2026. CC BY 4.0 License.

Competing interests

The contact author has declared that none of the authors has any competing interests.

Acknowledgements

We thank Ioana-Gianina Buda, PhD from Scribendi (www.scribendi.com) for editing a draft of this manuscript.

Financial support

The work described in this paper was fully supported by Independent Project of Key Laboratory of Xinjiang Coal Resources Green Mining, Ministry of Education(KLXGY-Z2612), Scientific Research Initiation Fund of Xinjiang Institute of Engineering (2025XGYBQJ38), National Natural Science Foundation of China (42474193), Special Funds for Jiangsu Science and Technology Plan (BE2022709).

References

Archie, G.: The electrical resistivity log as an aid in determining some reservoir characteristics, Transact AIME, 146: 54-62, 1942.

Attia, A.: Effects of petrophysical rock properties on tortuosity factor, J. Pet. Sci. Eng., 48(3-4). 185-198, https://doi.org/10.1016/j.petrol.2005.06.012, 2005.

Brace. W., and Orange A.: Electrical resistivity changes in saturated rocks during fracture and frictional sliding, J. Geophys. Res., 73(4), 1433-1445, https://doi.org/10.1029/JB073i004p01433, 1968.

Brace, W., Orange, A., and Madden, T.: The Effect of Pressure on the Electrical Resistivity of Water-Saturated Crystalline Rocks, J. Geophys. Res. Atmos., 70 (22), 5669-5678, https://doi.org/10.1029/JZ070i022p05669, 1965.

Chang, S., and Lee, C.: Estimation of cracking and damage mechanisms in rock under triaxial compression by moment tensor analysis of acoustic emission, Int. J. Rock Mech. Min. Sci., 41 (7), 1069-1086. https://doi.org/10.1016/j.ijrmms.2004.04.006, 2004.

Chen. F., Jin. A., and Liao, C.: Directional characteristic of resistivity changes in rock of original resistivity anisotropy, Chin. J. Geophys., 46, 271-280, 2003. (in Chinese)

Clavier, C., Coates, G., and Dumanoir, J.: Theoretical and Experimental Bases for the Dual-Water Model for Interpretation of Shaly Sands, Soc. Petr. Eng. J., 24(02), 153-168, https://doi.org/10.2118/6859-PA, 1984.

https://doi.org/10.5194/egusphere-2026-433
Preprint. Discussion started: 13 February 2026
© Author(s) 2026. CC BY 4.0 License.

Falcon-Suarez, I., Amalokwu, K., Delgado-Martin, J., Callow, B., Robert, K., North, L., Sahoo, S., and Best, A.: Comparison of stress-dependent geophysical, hydraulic and mechanical properties of synthetic and natural sandstones for reservoir characterization and monitoring studies, Geophys., Prospect, 67 (4), 784-803, https://doi.org/10.1111/1365-2478.12699, 2019.

Germanovich, L., and Dyskin, A.: Fracture mechanisms and instability of openings in compression, Int. J. Rock Mech. Min. Sci., 37(1-2), 263-284, https://doi.org/10.1016/S1365-1609(99)00105-7, 2000.

Glover, P., Hole, M., and Pous, J.: A modified Archie's law for two conducting phases, Earth Planet, Sci. Lett., 180(3), 369-383, https://doi.org/10.1016/S0012-821X(00)00168-0, 2000.

Han, T.: An effective medium approach to modelling the pressure-dependent electrical properties of porous rocks, Geophys. J. Int., 214(1), 70–78, https://doi.org/10.1093/gji/ggy125, 2018.

Healy, D., Jones, R., and Holdsworth, R., New insights into the development of brittle shear fractures from a 3-D numerical model of microcrack interaction, Earth Planet. Sci. Lett. 249(1-2), 14-28, https://doi.org/10.1016/j.epsl.2006.06.041, 2006.

Jia, P., Lei, L., Liu, D., Wang, X., and Wang, D.: Insight into Rock Crack Propagation from Resistivity and Ultrasonic Wave Variation, Theor., Appl., Fract., Mec., 109, 102758, https://doi.org/10.1016/j.tafmec.2020.102758, 2020.

Katayama, I., Aoi, Y., Tanimoto, K., Akamatsu, Y., Sawayama, K.: Simultaneous electrical resistivity and elastic wave velocity measurements during triaxial deformation of granite under brine-saturated conditions. Earth Planets Space, 75: 1-9. https://doi.org/10.1186/s40623-023-01809-4, 2023.

Lemaitre, J.: How to use damage mechanics, Nucl. Eng. Des., 80(3), 233-245, https://doi.org/10.1016/0029-5493(84)90169-9, 1984.

Li, J., Wang, M., Xia, K., Zhang, N., and Huang, H.: A Time-dependent dilatancy for brittle rocks, J. Rock Mech. Geotech., 9(6), 1054-1070, https://doi.org/10.1016/j.jrmge.2017.08.002, 2017.

Li, L., Jiang, M., and Zhang, F.: Quantitative simulation of triaxial test considering residual strength on deep rock using DEM and parameter analysis, Rock Soil Mech., 39(03): 1082-1090, 2018. (in chinese)

Li, W., Zou, C., Wang, H., and Peng, C.: A model for calculating the formation resistivity factor in low and middle porosity sandstone formations considering the effect of pore geometry, J. Pet. Sci. Eng., 152, 193-203, https://doi.org/10.1016/j.petrol.2017.03.006, 2017.

Liu, T., Li, Q., Zhang, C., Yang, W., Liu, S., and Zhao, W.: Studies and Applications of Dual Pore Saturation Model Based on Pore Structure Classification in Tight Reservoirs, Front Earth Sci., 9, 802842, https://doi.org/10.3389/feart.2021.802842, 2022.

https://doi.org/10.5194/egusphere-2026-433
Preprint. Discussion started: 13 February 2026
© Author(s) 2026. CC BY 4.0 License.

Lockner, D., Byerlee, J., Kuksenko, V., Ponomarev, A., and Sidorin, A.: Chapter 1 Observations of Quasistatic Fault Growth from Acoustic Emissions, International Geophysics, 51, 3-31, https://doi.org/10.1016/S0074-6142(08)62813-2, 1992.

Nie, L., Wang, C., Liu, Z., Xu, Z., Sun, X., Du, Y., and Wei, W.: An integrated geological and geophysical approach to identify water-rich weathered granite areas during twin tunnels construction: A case study, Tunn. Undergr. Sp. Tech., 135, 105025, https://doi.org/10.1016/j.tust.2023.105025, 2023.

Oh, S.: Geostatistical integration of seismic velocity and resistivity data for probabilistic evaluation of rock quality, Environ. Earth Sci., 69, 939–945, https://doi.org/10.1007/s12665-012-1978-3, 2013.

Parkhomenko, E., and Bondarenko, A.: Effect of uniaxial pressure on electrical resistivity of rocks Bull, Acad. Sci. USSR Geophys. Ser., 2: 326, 1960.

Qu, C., Xue, Y., Su, M., Qiu, D., Ma, X., Liu, Q., and Li, G.: Quantitative modeling of rock electrical resistivity under uniaxial loading and unloading, Acta Geophys., 72, 195–212, https://doi.org/10.1007/s11600-023-01101-9, 2024.

Reches, Z., and Lockner, D.: Nucleation and growth of faults in brittle rocks, J. Geophys. Res. Solid Earth, 99(B9), 18159-18173, 1994.

Rembert, F., Jougnot, D., and Guarracino, L.: A fractal model for the electrical conductivity of water-saturated porous media during mineral precipitation-dissolution processes, Adv. Water Resour., 145, 103742, https://doi.org/10.1016/j.advwatres.2020.103742, 2020.

Ren, J., Song, L., Wang, Q., Li, H., Fan, J., Yue, J., and Shen, H.: Development of multi-field rock resistivity test system for THMC, Solid Earth, 14, 261–270. https://doi.org/10.5194/se-14-261-2023, 2023.

Rowe, P.: The stress-dilatancy relation for static equilibrium of an assembly of particles in contact, Phil. OS. T. R. SOC. A., 269(1339), 500-527, 1962.

Shapiro, S., and Kaselow, A.: Porosity and elastic anisotropy of rocks under tectonic stress and pore-pressure changes, Geophysics, 70(5), N27-N38, https://doi.org/10.1190/1.2073884, 2005.

Song, M., Hu, Q., Liu, H., Li, Q., Zhang, Y., Hu, Z., Liu, J., Deng, Y., Zheng, X., and Wang, M.: Characterization and Correlation of Rock Fracture-Induced Electrical Resistance and Acoustic Emission, Rock Mech., Rock Eng., 56, 6437–6457, https://doi.org/10.1007/s00603-023-03376-2, 2023.

Terzaghi, K.: The shearing resistance of saturated soils and the angle between the planes of shear, Proc. Int. Conf. on Smfe ., 54 - 56, 1936.

https://doi.org/10.5194/egusphere-2026-433
Preprint. Discussion started: 13 February 2026
© Author(s) 2026. CC BY 4.0 License.

Wang, H., Xu, W., Jia, C., Cai, M., and Meng, Q.: Experimental Research on Permeability Evolution with Microcrack Development in Sandstone under Different Fluid Pressures. J. Geotech. Geoenviron. Eng., 142(6), 4016014, https://doi.org/10.1061/(ASCE)GT.1943-5606.0001462, 2016.

Zhang, J., Wu, X., Yang, X., Du, W., and Yue, M.: Observational evidence of anisotropic changes of apparent resistivity before strong earthquakes, Geophys. J. Int., 210(3), 1323–1331, https://doi.org/10.1093/gji/ggx235, 2017.